Journal of Microscopy, Vol. 221, Pt 2 February 2006, pp. 145–151
Received 2 August 2005; accepted 17 November 2005

Laser autofocusing system for high-resolution cell biological imaging

Y. LIRON, Y. PARAN, N. G. ZATORSKY, B. GEIGER & Z. KAM
Molecular Cell Biology, Weizmann Institute of Science, Rehovot 76100, Israel

Summary

Automated acquisition of high resolution, light microscope images of cells is becoming a common requirement in modern proteomic and cellomic research. A prerequisite for such microscopy is fine focus tuning, commonly optimized by multiple exposures, followed by image sharpness analysis. We describe here an extremely fast and accurate laser autofocusing system with distinct advantages for large-scale cell-based screening.

Introduction

The overwhelming molecular and structural complexity of biological systems requires the design and application of novel experimental approaches to test multiple cellular responses to a variety of external and genetic perturbations. These include over-expression of multiple genes, suppression of gene expression using RNA interference and application of large chemical libraries. Such assays typically use multiwell plates, and involve acquisition of many images in each well (Huh *et al.*, 2003; Yarrow *et al.*, 2003; Perlman *et al.*, 2004; Conrad *et al.*, 2004; Tanaka *et al.*, 2005). Different automated microscopes (e.g. ArrayScan, Cellomics, ImageXpress and Discovery1) have recently been developed for such screens but a major difficulty, shared by most systems, is the focusing technology, which is usually slow and relies on substrate flatness. This is particularly critical when the phenotype of interest involves high-resolution information. In order to resolve subcellular details, it is necessary to set the objective height, Z, to focus on the cells with accuracy defined by the focal depth, which is of a submicrometre scale for high-numerical aperture objectives. Such accuracy is far beyond the flatness of the bottom surface of multiwell plates (Fig. 1a). In addition, typical high-performance XYZ stages cannot move over large distances in XY while keeping the Z coordinate within the submicrometre tolerance. Therefore, the autofocusing solutions offered by commercially available systems do not work satisfactorily for high magnifications, are usually too slow and have high failure rates.

Correspondence to: Prof. Zvi Kam. Tel.: 972 8 934 3473; fax: 972 8 934 4125; e-mail: zvi.kam@ weizmann.ac.il

To address these needs we have developed a fast and accurate method for locating the focus, employing an accessory red laser beam and using the confocality principle. Similar to the mode of operation of a CD player, we defined the focus of the objective lens by maximizing the reflected light signal detected behind a pinhole. Laser autofocus devices are commonly utilized in the chip industry. They maintain the focus of reflective samples by a feedback control loop that maximizes the laser intensity (e.g. Autofocus attachment, Prior, Cambridge, UK). However, the application to cell biology (e.g. cultured cells seeded on glass cover slips) needs to cope with multiple-reflection interfaces between the objective and the specimen, each with different reflectivity, and to recognize the cell-substrate level with high axial resolution. We therefore based our focus determination on computerized analysis of the whole reflected intensity vs. focus height dependence curve. The laser autofocus has been installed in two different microscopes with direct mechanical and precise electronic focus mechanisms, and the focusing procedure was adapted for a wide range of plates and repeated in high-resolution cell-based screening applications before acquiring each image, adding a negligible time to the fluorescence exposures. We believe that this key component in automated microscopy opens new opportunities in high-throughput acquisition of detailed subcellular information.

Materials and methods

Description of the laser autofocus optical system

A schematic optical path and position of the various optical components are shown in Fig. 2. A laser (Uniphase 2-mW HeNe, no. 1) emitted a beam of light (solid rays) that was expanded (1.5-mm focus CD player lens and 30-mm singlet separated by 31.5 mm) to fill the objective back aperture (no. 2). Filling the back aperture guaranteed that the laser depth-of-focus would be identical to that of the imaging process, which was automatically maintained when exchanging objectives. The expanded beam was then reflected into the microscope optical axis by a specially designed selective mirror that acted as a notch reflector for the laser wavelength, and was transparent to all other colours. (633DCRB stock no.

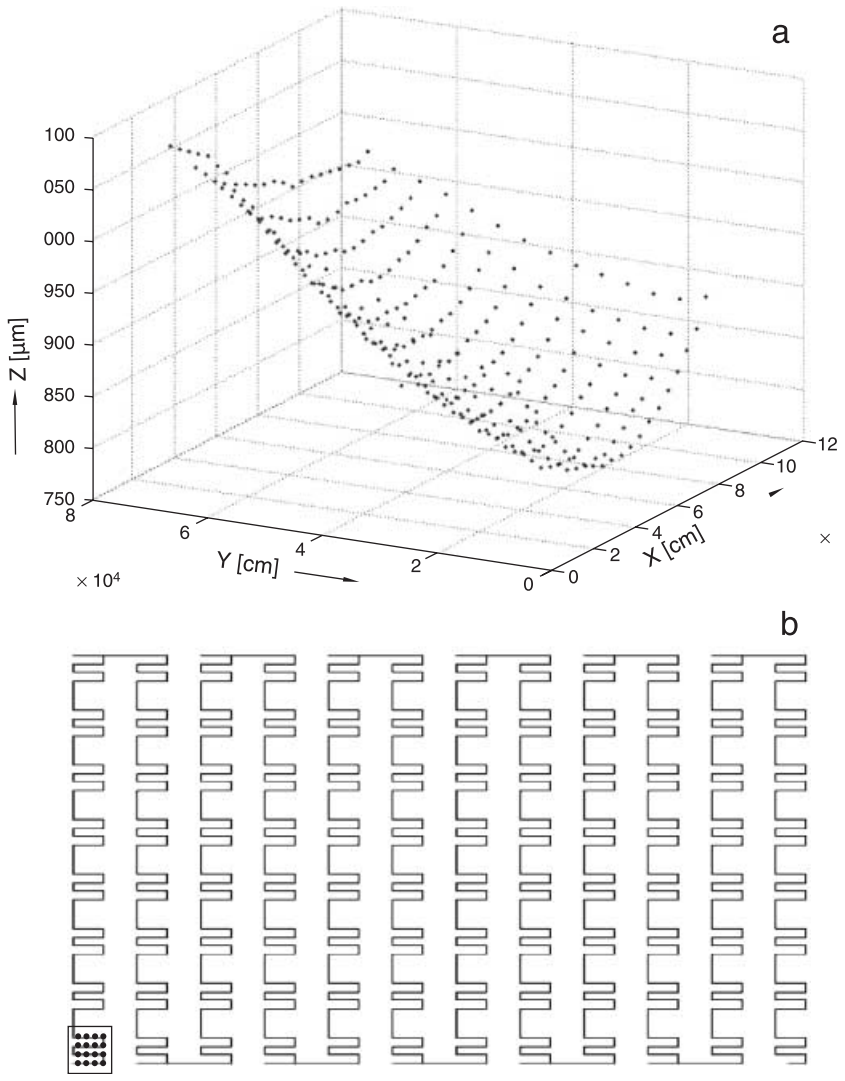

Fig. 1. (a) The height of the multiwell plate bottom surface (SensoPlate™, cat. no. 60-781091, Greiner Bio-One, Frickenhausen, Germany) measured at a regular array of points. In addition to plan tilt (~200 µm), which is different for each plate due to imperfect production and irreproducible positioning on the XY stage, a curved bottom shows ~100-µm deviations from a plane and these deviations vary in magnitude and shape from plate to plate, and for the same plate after incubation at 37 °C for cell culturing. (b) The optimized scanning XY path in a 96-well plate. Here 16 imaged fields are visited in each well. The path minimizes distances between fields, drastically speeding the autofocus searches. Two parameters define the fraction of the well area around its centre to be scanned and the (linear) fill factor of the images (> 1 for partly overlapping fields). Well A1 walls are schematically marked with the centres of 4 × 4 fields.

23416, no. 3 Chroma, VT 05101). The laser beam was focused by the objective (no. 4). We adjusted the position of the laser beam expanding lenses so that the laser was focused on a reflecting surface while sharply imaging scratches on it. Part of the light was reflected by the sample substrate surfaces back into the optical path (broken light rays, no. 5) and out from the imaging path by the notch reflector (no. 3) towards a beam splitter (no. 6) diverting 50% of these reflections into a focusing lens, a confocal pinhole (no. 7) and a Planar Diffused Silicon Photodetector (PIN diode) with Field Emission Transistor (FET) amplifier (no. 8). The voltage was digitized (PCI-6023E, National Instruments, TX, USA) and read into the computer that also controlled the focus drive (ProScan, Prior). The laser light could be switched off during fluorescent or bright-field imaging by a shutter (no. 9). If laser wavelength transmission through the emission filter was sufficiently low (e.g. for blue and green fluorescence but usually not for yellow and red fluorescing specimens) images could be taken with the laser light on. In principle, imaging of the laser beam spot pattern could be used to find the focus, which can be easily built into microscopes with digital cameras (e.g. in the laser autofocus of Discovery-1, Universal Imaging, Downingtown, PA) but the focusing process is much slower. The optical system was constructed using microbench components (Spindler & Hoyer, Goettingen, Germany) on the microscope table and coupled to the microscope optical path via a slider (no. 10 and Insert in Fig. 2) housing the notch reflector and a mirror. It was inserted below the objective into the slot usually holding the differential interference contrast prism. This setup coupled the laser optics and the microscope, allowing free objective movement.

Results

The fraction of laser intensity reflected at an interface, R, is roughly proportional to the square of the refractive index difference [for perpendicular incidence on the interface between

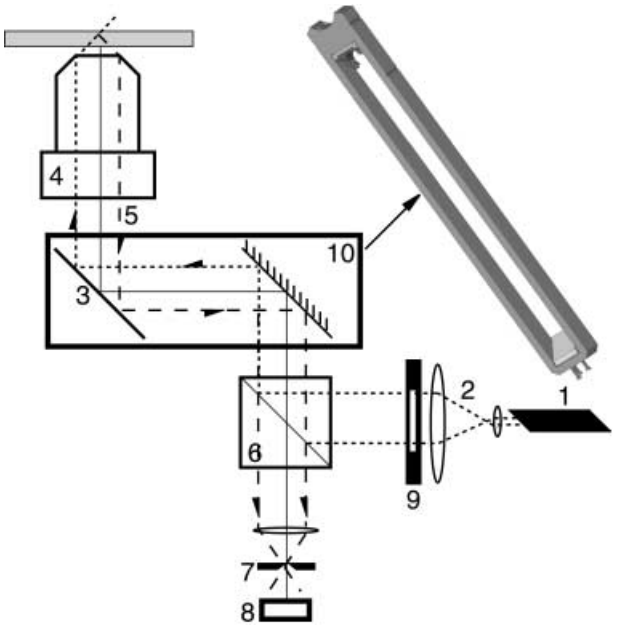

Fig. 2. The autofocus optical system. See detailed description of the components in the text. Insert: the CAD image of the slide coupling the expanded laser beam into the microscope optics.

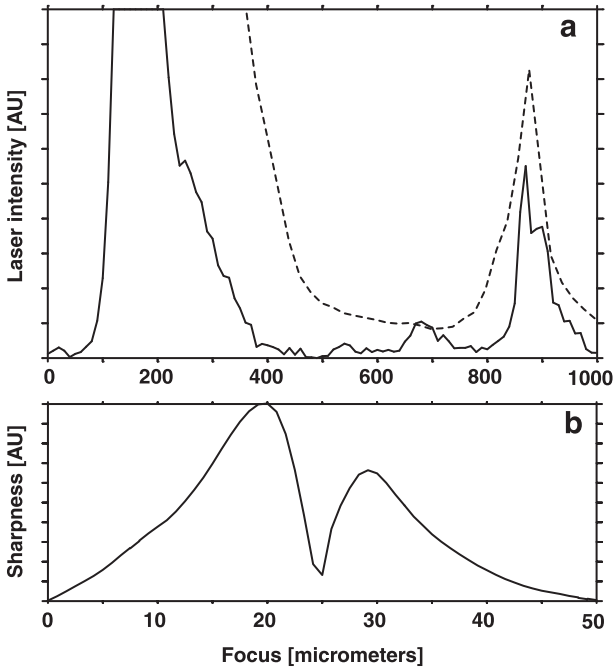

Fig. 3. Laser intensity vs. focus height. (a) 100- and 200-μm pinholes (solid and dashed lines, respectively). The intensity values are digitized and peak maxima define the bottom and top interfaces of the substrate with air and sample buffer, respectively. (b) Sharpness, calculated as the averaged magnitude of local derivatives from phase contrast images taken with 60×/0.9 objective. The dependence on defocus displays higher values above and below the focus and a local minimum at the focus.

media with refractive indices $n2$ and $n1$, $R = \{(n2 - n1)/(n2 + n1)\}^2$]. For biological specimens located in water (or aqueous buffers) behind glass cover slips, reflection from the substrate glass–air interface (closer to the objective) is about 4% of the incident beam, and only about 0.4% from the glass–water interface. Similar values apply to the optical-quality bottoms of plastic multiwell plates. A scan of the reflected laser intensity vs. focus showed two strong and weak peaks (Fig. 3a). The width of the peaks could be broadened by opening the confocal pinhole aperture in front of the detector. Although, in principle, a broader peak apparently reduced the accuracy of focusing, it smoothed the effects of interference speckles and of Airy rings crossing the pinhole, yielding a peak shape that was easier to analyse (dotted curve, Fig. 3a). By contrast with the sharp reflected intensity peak, phase contrast images, particularly at high magnifications, displayed higher contrast above and below the focus (showing black or white features for over- or under-focusing) with lowest contrast in focus. A typical phase-image sharpness profile based on derivatives, often used as an optimization criterion in image-based autofocusing algorithms, indeed displayed double-peaked behaviour near the focus (Fig. 3b).

As the reflected laser intensity from air below the substrate was very low, the air–substrate strong peak was characterized by a very high signal-to-background value and was the first peak to be detected when moving from below the substrate height. Its position yielded an approximation to the position of the water interface at the other side of the substrate where cells grew. However, typical variations in cover slips or plate-bottom thickness can reach several micrometres over short distances and thus the detection of the air–substrate interface is not a sufficiently accurate reference for subcellular imaging applications at high magnification. We therefore divided the autofocus procedure into two stages, where only the fast, second stage was repeated before every image acquisition. During the first stage ('long peak detection search') the focus was moved fast towards the specimen, starting about 200 μm below the bottom substrate height, while the laser intensity was continuously monitored (every 20 μs). On-the-fly analysis updated the highest occurring reflected intensity and its position. Once a maximum was passed and intensity fell below half, the peak height was checked, centre position was estimated as the mean between left and right half-height positions, and the Z position of the second peak was estimated by adding the substrate thickness. As the long search continued, the second peak was encountered. This was 'certified' by its maximum intensity, width and contrast to nearby minima, and its closeness to the anticipated Z, to be about the set value otherwise the long search continued or stopped with a failure flag if the objective height approached the working distance, to avoid hitting the sample. This procedure ignored spurious reflection peaks, often originating from within plastic substrates, or optical perturbations due to scratches. The long

search algorithm required an estimated substrate thickness, peak maximum intensity, objective working distance, and an initial estimate for the focus. Wide variability was permitted (i.e. 50% in peak maxima, 50 μm for thickness). These parameters could be adjusted during interactive monitoring of the focusing performance before launching an automated procedure. As operating systems (we used Linux) are not real-time controllers, we added a time stamp to each laser intensity reading, and we repeated the focus scan for the scarce events of long time gaps near the peaks (due to system occupation by utility tasks).

The high speed of the long search limited the accuracy of the estimated peak maximum Z. At the second stage ('local peak search') the precise position of the maximum intensity was searched around the estimated Z (typical range ±10 μm for 60× and ±100 μm for 10× objective) and focus was positioned at the maximum, or any selected 'delta' distance from it. The range of search should be several times larger than the expected focus changes between successive imaged fields (or drifts in time) and should cover the peak intensity fall to 20–30% from the maximum at both sides. As we did not attempt to fit a model to the peak shape there was no gain in accuracy by recording the full peak width. However, we found increasing errors in the position of peaks that lay close to the edges of the range of search. We therefore shifted the local search range or repeated the long search procedure and re-estimated the local search range, depending on how far the peak maximum was from the centre of the range. The search algorithm was differently applied to our two systems depending on the microscope focus control mechanism. For the highly reproducible but slow focus control of the IX81 microscope (Olympus, Tokyo, Japan) we measured the peak intensities at 11 points and fitted a parabola and position Z to the fitted curve maximum. The fit overcame noise and was governed by the intensity fall on both sides of the maximum. For the IX70 microscope we found the mechanical focus with backlash correction to be sufficiently reproducible within the 20-μm range of the local search. We identified the peak maximum after sampling the laser intensity at this local range and repositioned Z. This method yielded accurate focus positioning with ±0.1 μm reproducibility for the IX81 microscope (±0.3 μm for IX70) and better than ±0.5 μm precision in absolute focusing at the top substrate surface, as judged by imaging fluorescently labelled focal adhesions in cultured adherent cells examined with a 60×/0.9 objective (see below). An adjustable delta value allowed the focus to be brought to any height above the substrate before acquiring an image. For example, cell nuclei and associated organelles (mitochondria and endoplasmic reticulum) were best seen 2–4 μm above the substrate level. The delta could also compensate for axial chromatic shifts between the red laser and the fluorescence emission wavelength.

For low magnifications (< 20×) it was not easy to resolve the two reflection peaks, as the weaker peak appeared as a small shoulder flanking the strong peak. The autofocusing process then estimated the maximum of the main peak and set the focus after adding the slide thickness. This was sufficiently accurate for low magnification due to the large focal depth.

Usually, during scan of images in nearby fields, the position of the last focus was an excellent approximation about which the local search was performed. Only when the maximum signal position drifted away from the centre of Z search (typically the middle one-third range) or when consecutive fields were far away from each other in XY was the long search repeated to reidentify the two reflection peaks. The plate-scanning path was optimized for minimal distance between imaged fields to reduce the need for the long searches (Fig. 1b). This procedure allowed automated acquisition of thousands of high-resolution images without manual intervention. Failure rates were below 0.1%, usually resulting from local severe defects or scratches in the substrate surfaces. In this system the major contribution to the total screen duration was the fluorescence exposure times, rather than plate scan movements, autofocusing, or image storage, which were performed simultaneously when possible (e.g. storing the last image to disk while exposing the next one). For multiple position time-lapse experiments, the positions selected for repeated revisiting may be far from each other but the focus found at the last time point was used as an initial reference for the local focus search, making it possible to revisit hundreds of positions every few minutes without being affected by thermal and mechanical drifts.

In Fig. 4a we show a montage (imaged fields are tiled together) assembled from an automatic scan of a 384-well plate with REF52 cells stably expressing Paxillin-YFP fusion protein. Paxillin was localized at cell-substrate focal adhesions, demonstrating the quality of focusing. The cells were scanned using a ×60/0.9 air objective with a correction collar adjusted for the plate-bottom thickness. The full magnification images (Fig. 4b) display the fine structure of the focal adhesions at 0.3-μm resolution. The typical throughput of the screening system reached ~0.2 terabytes/week.

This autofocus method had another advantage for high-throughput imaging of cell patterns that were distributed three-dimensionally throughout the cell volume. The precise definition of the substrate position provided an exact reference for the bottom focus plane of thick samples. Detailed three-dimensional data could be obtained by optical sectioning followed by deconvolution and reconstruction, which was incompatible with high-throughput screening. Lateral cell dimensions were 100 times the XY resolution but the thickness of tissue-culture cells was only several times the Z resolution of objectives. Image projections were therefore almost as informative as the full three-dimensional data for many applications. We therefore directly acquired the projected image in our system by integrating on the camera detector while the focus was moved at a constant speed from 2–3 μm below the bottom of the specimen toward 2–3 μm above its top ('sweeping focus procedure'). In order to deblur out-of-focus contributions we applied fast (processing time of 1–3 s) two-dimensional deconvolution using the projected point-spread

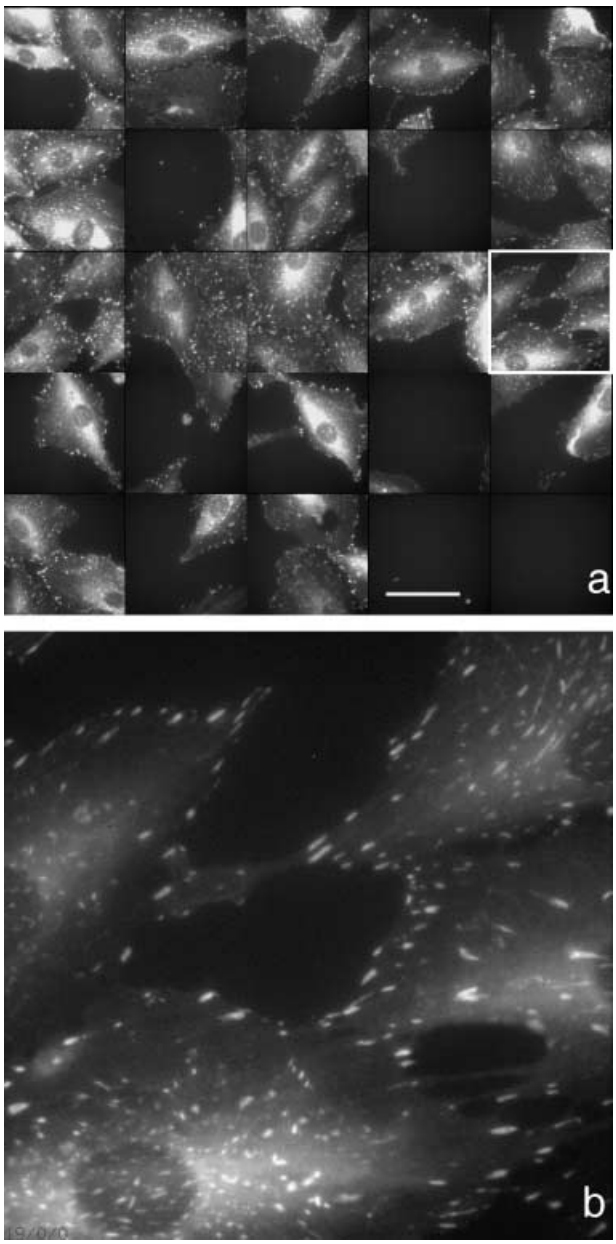

Fig. 4. Cell-substrate adhesions in REF52 cell line stably expressing YFP-tagged Paxillin. (a) Montage of tiled images taken in a well. (b) Full resolution image. This specimen serves as a critical test for the autofocus procedure as < 1 μm shift in focus is clearly manifested in the recorder image resolution.

function. The computational projection of four-dimensional data (three-dimensional + time-lapse) followed by two-dimensional deconvolution was used long ago by Hiraoka *et al.* (1989) in order to reduce the processing time. Here we extended this method to the actual acquisition process. The resulting image displayed a sharp projection of the entire three-dimensional cell volume. The information content was comparable to three-dimensional deconvolution of the three-dimensional image followed by projection but required considerably less time both in the acquisition and processing of the images (seconds instead of minutes). The depth information within the sample was lost but all features within the swept depth were sharply displayed and their fluorescent intensities were correctly presented, an important feature for quantitative analysis. Visual information about Z-axis variations could be retrieved by the acquisition of two sweeping focus images during translation of the specimen stage in two opposite directions ($\pm x$), a process equivalent to the creation of a stereo-pair (Hiraoka *et al.*, 1989; Cheng *et al.*, 2000).

We demonstrated here the sweeping focus projections by imaging mitochondria in SV80 cells expressing a YFP-tagged mitochondria-localization probe (EYFP-Mito, Clontech, Mountain View, CA, USA). The morphology of the mitochondria was highly convoluted and changed with fast dynamics. The sweeping-focus acquisition allowed grabbing of this three-dimensional structure with minimal motion smear. Deconvoluted sweeping focus images are presented in Fig. 5. The convolution kernel was computed from synthetic projection of the three-dimensional point spread function of Stokseth (1969) and plotted overlayed on the image. For simulated data composed of points, lines and planes we found excellent comparison between three-dimensional deconvolution followed by projection and first projection followed by two-dimensional deconvolution (data not shown).

Discussion

We have developed a fast and accurate laser autofocusing method especially useful for high-throughput applications of automated high-resolution microscopy. This method provides numerous advantages when compared with commonly used image-based autofocusing methods optimizing image sharpness.

Image-based autofocusing is slow. Even when real-time processing is performed using video-rate imagers (which have low performance with low light level fluorescence imaging) the multiple image acquisition time takes several seconds. Our method is very fast, as fast as the mechanical focus adjustment. For example, objective piezo-mounts have a millisecond focus setting time. We have successfully applied mechanical focus drive with a 0.2-s focusing time.

Different algorithms, defining sharpness from frequency and real space analysis, have been used (Geusebroek *et al.*, 2000). To accelerate the process, the search can first be made in large steps and refined until the required focus accuracy is reached. For example, in Fibonacci minimization [or simplex (Flannery *et al.*, 1986)] a 12-step search over a 0.2-mm range will define the minimum with 0.3 μm tolerance. However, such an algorithm works only for functions that are monotonously decreasing towards the minimum. To the best of our knowledge there is no evaluation scheme that can map distance from focus into a smooth monotonous dependence over

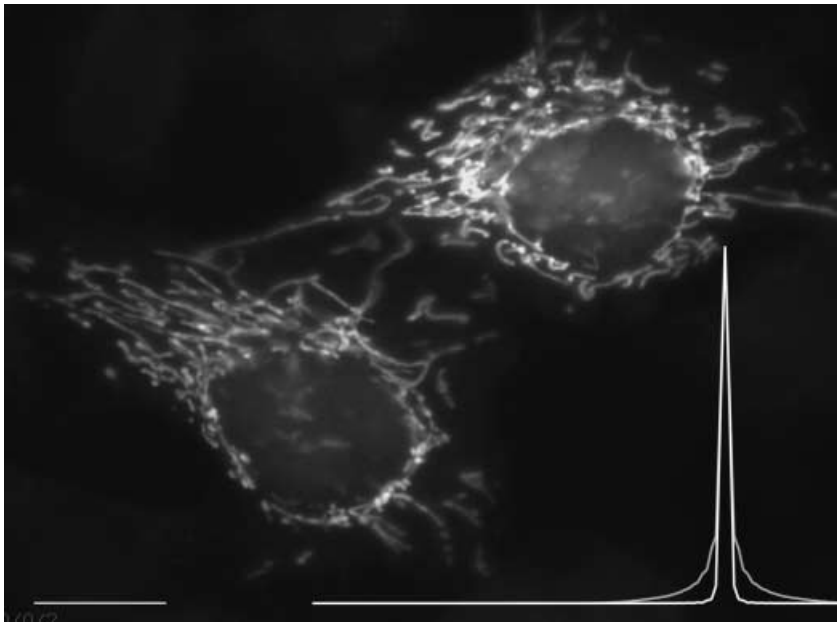

Fig. 5. SV80 cells transfected with mitochondrial localization vector and imaged by sweeping focus projection followed by two-dimensional deconvolution. Overlay: the radial profiler of the projected point-spread function (PSF) used for the deconvolution (wide curve) next to the the in-focus PSF (narrow curve).

ranges much larger than the focal depth, as needed for scanning plates. Scans must therefore start close to the focus (typically within 10 μm) and refine the position. When the starting Z is not close to the true focus, some spurious focus is likely to be found. Even close to the true focus, sharpness functions have multiple maxima. In addition, the walls around each well cast shadows distorting the phase ring illumination cone so that contrast strongly depends on the position within the well. Nomarski's differential interference contrast is not easy to apply in multiwell plates although, if used, it displays better definition of sharpness at the focus of thin samples. However, for typical cells the contributions to sharpness may be dominated by either lamellipodia at the periphery or by nuclear-related features, depending on cell type and density. Live cell focus would therefore reach an undefined focal plane somewhere within the cell height, yielding 3–6 μm uncertainty. Sharpness criteria are very sensitive to dirt and scratches on surfaces. Glass slides or plastic well bottoms are a fraction of a millimetre thick and often cause autofocus procedures based on maximal sharpness to find the wrong side of the sample substrate. On the other hand, the in-focus reflected laser intensity signal is strong, falls sharply away from the focus, and has a well-defined magnitude that is independent of the sample and therefore can be uniquely identified during very fast focal sweeps. The difference between the reflected intensities at the bottom (air–substrate) and top (substrate–water) interfaces allows the reliable identification of the two peaks and positioning of the focus at exactly the substrate–water interface (or at any plane above it).

Sharpness algorithms, which are commonly used for autofocusing, are context dependent. Thus, it is difficult to define a common criterion that can apply to a wide variety of specimens. In addition, assays also need to account reliably for empty fields, thus enabling accurate measurements of cell loss due to toxic treatments, cell detachment or cell death. Sharpness criteria cannot be applied when no cells are found within the imaged field and may lead to loss of focus. Laser reflection, on the other hand, is independent of cells growing on the substrate.

Image-based focus search can be effective in principle in fluorescence microscopy but cannot be applied repeatedly due to bleaching. Live cell samples also require the minimization of phototoxicity, eliminating use of multiple exposures as a way to define the focus. The laser autofocusing process does not expose the sample to bleaching or photo-damage and is therefore ideally suited for live samples, such as green fluorescence protein (GFP) tagged live cells.

The process of adjusting the objective correction collar to minimize aberrations due to substrate thickness is critical for imaging in plastic plates, as the bottom surface thickness varies greatly between producers. Collar adjustment is associated with focal shift. The autofocus follows this shift during collar adjustment, tremendously accelerating and simplifying this procedure.

Last but not least, the laser autofocus defines the bottom height for thick samples. 'Sweeping focus' acquisition practically extends the depth of focus throughout the cell height and offers a huge speed factor in both imaging and analysis. Mathematically, convolution and projection are linear commutative operators. However, the inverse operation of deconvolution, applied to light microscope images by iterative constrained deconvolution (Agard & Sedat, 1983; Agard, 1984; Swedlow *et al.*, 1997), is not a linear operator and the commutative property between projection and deconvolution

is not rigorous. Nevertheless, the criteria of the uniqueness of the deconvolved solution and the expected errors were theoretically bounded (Schafer *et al.*, 1981; Sezan & Stark, 1982). Although errors are not easy to estimate in practice, the stability of inversion by constrained deconvolution is well established. Three-dimensional deconvolutions were applied to a large amount of image data in light microscopy and two-dimensional deconvolutions were widely used in astronomy (Jansson, 1997). One must keep in mind that the bit depth in digital image acquisition is an important factor to be considered. 12-bit images with MHz digitizers and low noise charge-coupled device (CCD) detectors are common today and are mandatory for effective three-dimensional deconvolutions, in order to record in- and out-of-focus contributions within the CCD dynamic range. For an integrating sweeping focus image to be strictly identical to computational projection of typical 16–64 optical sections, each close to the saturation level, the well depth and the corresponding digitation depth should be 4–6 bits higher, i.e. 16 bits. This feature is available for some new CCDs with low readout noise (Daigle *et al.*, 2004). In screening applications the fluorescence levels and exposure times acquire far below saturation images and the sweeping focus mode performs well with 12-bit cameras. It is extremely useful in high-throughput quantification of the expression level of proteins and is also useful for dynamic studies of mitochondria, endoplasmic reticulum or vesicle transport in live cells, avoiding loss of data when compromising for a sparse set of focal sections to allow fast temporal sampling.

We have applied the autofocusing method to high-resolution applications. Its performance allows a considerable increase in the quality and throughput of image acquisitions in dense multiwell plates compared with existing commercial systems, making the fluorescence exposure time the major time-consuming step. We have also applied the autofocus to acquisition on slides, as well as for fast tiling of high magnification images to cover selected areas larger than the field accepted by the camera. The optics, computer digitation card and software are adaptable to most microscopes and to various substrate slides and plate bottoms. We expect that autofocusing will be integrated into common computerized microscopes, enhancing their manual usability and ease of precise focusing as well as their automated acquisition capability of high resolution images.

Acknowledgements

Research supported by BSF 2001221, Ministry of Science 262, the Yad Avraham Center for Tumor Diagnosis and Treatment, the Clore Center for Biological Physics and the Kahn Fund for system biology at the Weizmann Institute of Science. ZK is the Israel Pollak Professor in Biophysics.

References

Agard, D.A. (1984) Optical sectioning microscopy: cellular architecture in three dimensions. *Ann. Rev. Biophys. Bioeng.* **13**, 191–219.

Agard, D.A. & Sedat, J.W. (1983) Three-dimensional architecture of a polytene nucleus. *Nature*, **302**, 676–681.

Cheng, Y., Hartemink, C.A., Hartwig, J.H. & Forbes Dewey, C. Jr (2000) Three-dimensional reconstruction of the actin cytoskeleton from stereo images. *J. Biomechanics*, **33**, 105–113.

Conrad, C., Erfle, H., Warnat, P. *et al.* (2004) Automatic identification of subcellular phenotypes on human cell arrays. *Genome Res.* **14**, 1130–1136.

Daigle, O., Gach, J.-L., Guillaume, C., Carignan, C., Balard, P. & Boissin, O. (2004) *SPIE Conference Proceedings*, Vol. 5499. Optical and IR Detectors for Astronomy, Glasgow, UK, 21–24 June 2004. http://arxiv.org/abs/astro-ph/0407315.

Geusebroek, J.-M., Cornelissen, F., Smeulders, W.M. & Geerts, H. (2000) Robust autofocusing in microscopy [and references 1–8, 10–11, 25–26 cited therein]. *Cytometry*, **39**, 1–9.

Hiraoka, Y., Minden, J.S., Swedlow, J.R., Sedat, J.W. & Agard, D.A. (1989) Focal points for chromosome condensation and decondensation revealed by three-dimensional in vivo time-lapse microscopy. *Nature*, **342**, 293–296.

Huh, W.-K., Falvo, J.V., Gerke, L.C., Carroll, A.S., Howson, R.W., Weissmann, J.S. & O'Shea, E.K. (2003) Global analysis of protein localization in budding yeast. *Nature*, **425**, 686–691.

Jansson, P.A. (ed.) (1997) *Deconvolution of Images and Spectra*. Academic Press, New York.

Perlman, Z.E., Slack, M.D., Feng, Y., Mitchison, T.J., Wu, L.F. & Altschuler, S.J. (2004) Multidimensional drug profiling by automated microscopy. *Science*, **306**, 1194–1198.

Press, H.W., Flannery, B.P., Teukolsky, S.A. & Vetterling, W.T. (1986) Downhill Simplex Method in Multidimensions. *Numerical Recipes: The Art of Scientific Computing*, pp. 289–293. Cambridge University Press, Cambridge.

Schafer, R.W., Mersereau, R.M. & Richards, M.A. (1981) Constrained iterative restoration algorithms. *Proc. IEEE*, **69**, 432–450.

Sezan, M.I. & Stark, H. (1982) Image restoration by the method of convex projection algorithms. *IEEE Trans. Med. Imag.* **MI-1 Oct.**, 95–101.

Stokseth, P.A. (1969) Properties of a defocused optical system. *J. Opt. Soc. Am.* **59**, 1314–1321.

Swedlow, J.R., Sedat, J.W. & Agard, D.A. (1997) Deconvolution in Optical Microscopy. *Deconvolution of Images and Spectra* (ed. by P. A. Jansson), pp. 284–309. Academic Press, New York.

Tanaka, M., Bateman, R., Rauh, D. *et al.* (2005) An unbiased cell morphology-based screen for new, biologically active small molecules. *Plos. Biol.* **3**, 1–13.

Yarrow, J.C., Feng, Y., Perlman, Z.E., Kirchenhausen, T. & Mitchison, T.J. (2003) Phenotypic screening of small molecule libraries by high throughput cell imaging. *Comb. Chem. High Thr. Screening*, **6**, 279–286.